Sodium-Ion Batteries

Deutsche Ausgabe: DOI: 10.1002/ange.201510978
Internationale Ausgabe: DOI: 10.1002/anie.201510978

Boosted Charge Transfer in SnS/SnO_2 Heterostructures: Toward High Rate Capability for Sodium-Ion Batteries

*Yang Zheng[+], Tengfei Zhou[+], Chaofeng Zhang, Jianfeng Mao, Huakun Liu, and Zaiping Guo**

Abstract: *Constructing heterostructures can endow materials with fascinating performance in high-speed electronics, optoelectronics, and other applications owing to the built-in charge-transfer driving force, which is of benefit to the specific charge-transfer kinetics. Rational design and controllable synthesis of nano-heterostructure anode materials with high-rate performance, however, still remains a great challenge. Herein, ultrafine SnS/SnO_2 heterostructures were successfully fabricated and showed enhanced charge-transfer capability. The mobility enhancement is attributed to the interface effect of heterostructures, which induces an electric field within the nanocrystals, giving them much lower ion-diffusion resistance and facilitating interfacial electron transport.*

Rechargeable sodium-ion batteries have received a great deal of research interest as a promising alternative to lithium-ion batteries, owing to the abundant resources and low cost of sodium.[1–3] Inspired by the existing lithium-ion battery technology, various attempts have been made to adapt anode materials for Li-ion chemistry to Na-based systems. Unfortunately, most of the investigated anode materials suffer from low specific capacity, poor rate capability, and shorter cycle life, because Na^+ ions have a larger ionic radius than Li^+ ions.[4,5]

Currently, searching for a suitable anode material with excellent performance to meet the increasing demands for large-scale energy-storage applications is still the major challenge. Although considerable research has been devoted to exploring new anode materials with high specific capacity or good cycling stability for application in Na-ion batteries,[6,7] rather less attention has been paid to the high-rate capacity which is an important aspect of performance for practical applications. Therefore, the rational design and controllable synthesis of anode materials with high-rate performance and superior cycle life are highly desirable. To obtain viable anode materials with high-rate capacity, it is particularly important to choose appropriate host materials with high theoretical sodium storage capacities as the building blocks. Among the limited Na-storage anode materials, SnO_2 has been extensively investigated owing to its high theoretical capacity (ca. 667 mA h g^{-1}) and abundance.[8,9] Practical applications of SnO_2 materials are limited, however, by its poor intrinsic conductivity, low initial coulombic efficiency, and inferior cycling stability.[10–12] Besides SnO_2, the unique layered structure with large interlayer spacing and high reversible capacity of SnS make it another highly promising candidate.[13,14] Compared to metal oxide anodes, the corresponding metal sulfide anodes have smaller band-gap energy and higher electrical conductivity, because of the more covalent metal–sulfur bond.[15,16] Furthermore, SnS has a higher reversibility than its equivalent oxide,[17,18] thus ensuring higher initial coulombic efficiency and reversible capacity.

Heterostructures have great potential applications ranging from high-speed electronics to optoelectronics devices because of their interface effects, which offer unprecedented properties at interfaces.[19–21] It has been demonstrated that creating heterostructures by coupling nanocrystals with different band gaps will enhance the surface reaction kinetics and facilitate charge transport due to the internal electric field at heterointerfaces.[22] Wang et al. reported the ultrafast charge transfer in the MoS_2/WS_2 heterostructures.[23] Walukiewicz et al. investigated the charge-transfer effects at the interfaces of CdO/SnTe heterostructures and found a 4-fold enhancement of the electron mobility, which can be attributed to reduction of the charge center scattering.[24] Shao et al. designed a TiO_2(B)-anatase structure with high Li storage capacity and superior high-rate performance, benefiting from the synergistic effects of the TiO_2(B)-anatase, which can promote Li^+ diffusion kinetics and enhance electronic conductivity.[25]

Thus, from the perspective of enhancing the electronic conductivity and sodium-ion diffusion capability of anode materials, the design and fabrication of a complex architecture by employing the SnS/SnO_2 heterostructure, might be a feasible strategy for obtaining the internal charge-transfer driving force, which will facilitate ion/electron diffusion during the cycling process. Herein, we proposed a unique architecture for amorphous carbon covered SnS/SnO_2 heterostructures anchored to graphene nanosheets, which exhibited a remarkable high-rate capability and ultra-long cycle life as an anode for sodium-ion batteries.

The formation procedure for the C@SnS/SnO_2@Gr architecture (Gr = graphene) is shown in Scheme 1. First, graphene oxide was synthesized by a modified Hummers' method. Second, tin oxide was grown onto the graphene by a hydrothermal method.[26] Subsequently, amorphous carbon was anchored to the SnO_2@Gr surface. Finally, C@SnS/SnO_2@Gr

[*] Y. Zheng,[+] T. F. Zhou,[+] C. F. Zhang, J. F. Mao, Prof. H. K. Liu, Prof. Z. P. Guo
Institute for Superconducting & Electronic Materials
University of Wollongong
Wollongong, NSW 2522 (Australia)
E-mail: zguo@uow.edu.au
Y. Zheng,[+] Prof. Z. P. Guo
School of Materials and Energy, Guangdong University of Technology
Guangzhou 510006 (China)
[+] These authors contributed equally to this work.

Supporting information for this article can be found under http://dx.doi.org/10.1002/anie.201510978.

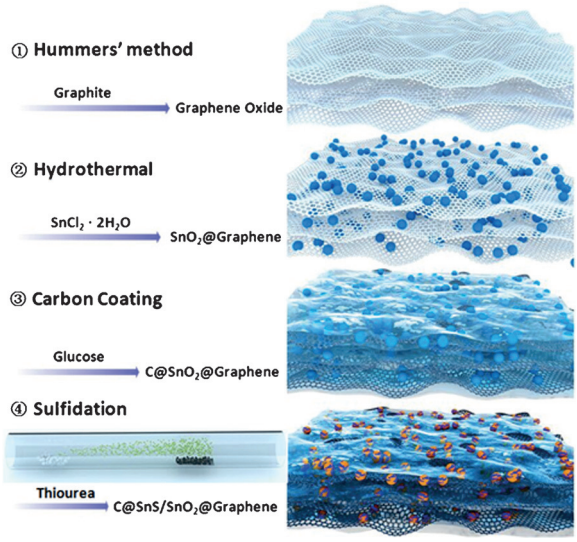

Scheme 1. Schematic illustration of the formation of the C@SnS/SnO_2@Gr architecture.

was obtained by a sulfidation process of as-prepared C@SnO_2@Gr with thiourea at 350 °C under argon condition.

The purity and crystalline phase of the samples were analyzed by powder X-ray diffraction (XRD). Figure 1 a presents XRD patterns of the C@SnO_2@Gr and C@SnS/SnO_2@Gr powders. All of the diffraction peaks in pattern A of Figure 1 a can be indexed to tetragonal rutile SnO_2, indicating that pure and single-phase SnO_2 was prepared. After sulfidation, apart from the SnO_2 diffraction peaks, some entirely new peaks are observed (pattern B in Figure 1 a), which can be assigned to the orthorhombic-SnS, and no peaks for other impurities are found, revealing the coexistence of SnS and SnO_2. Moreover, the broadened diffraction peaks in pattern B indicate that the ultra-small particle size was not increased after sulfidation.

Figure 1 b, and Figure S1 in the Supporting Information shows the Raman spectra of the as-prepared samples. As shown in Figure 1 b, three fundamental peaks can be observed at 473 cm^{-1}, 627 cm^{-1}, 767 cm^{-1} in both the C@SnO_2@Gr and the C@SnS/SnO_2@Gr materials, corresponding to the E_g, A_{1g}, and B_{2g} vibrations of SnO_2.[27,28] Moreover, three typical Raman scattering peaks at 161, 183, and 228 cm^{-1} are identified for the C@SnS/SnO_2@Gr sample, which can be attributed to the B_{3g}, B_{2g}, and A_g vibrational modes of SnS, respectively.[29,30] These peaks further confirm the successful formation of SnS in the C@SnO_2@Gr composite after the sulfidation process. Note that the intensities of peaks from the SnO_2 in the C@SnS/SnO_2@Gr sample are reduced, owing to the interaction between SnO_2 and the in situ generated SnS, which may diminish both the excitation laser and the emitted Raman signals.[28] X-ray photoelectron spectroscopy (XPS) was conducted to investigate the surface electronic states and chemical compositions of the synthesized samples (Figure 1 d, Figure S2). It can be seen that the C@SnO_2@Gr sample (the top curve in Figure 1 c) only contains the elements Sn, O, and C, with photoelectron peaks appearing at binding energies of 487 (Sn $3d_{5/2}$), 495 (Sn $3d_{3/2}$), 531 (O 1s), and 285 eV (C 1s), respectively.[30] Compared with the spectrum of C@SnO_2@Gr, two additional peaks at 163 eV (S 2p) and 228 eV (S 2s) can be found in the survey spectrum of the C@SnS/SnO_2@Gr sample, suggesting the successful incorporation of S into the C@SnO_2@Gr hybrid.[13] As shown in Figure 1 d, the two peaks of Sn 3d for C@SnS/SnO_2@Gr both shifted to lower binding energies, as a result of the coupling effect of SnO_2 (Sn^{4+}) and SnS (Sn^{2+}) in the SnS/SnO_2 heterostructures. The peaks of 495.3 eV and 486.9 eV are ascribed to Sn $3d_{3/2}$ and $3d_{5/2}$ of Sn^{4+}, respectively, while the peaks 494.3 eV and 485.9 eV should be assigned to Sn $3d_{3/2}$ and $3d_{5/2}$ of Sn^{2+}, confirming the formation of the SnS/SnO_2 heterostructures. Moreover, the Sn^{2+}/Sn^{4+} ratio measured with XPS analysis is estimated to be around 1.1, which is consistent with the result of EDS spectrum (Figure S3). After the sulfidation reaction, the in situ formation of SnS with the lower chemical valence and lower electronegativity of S occurred in close contact with SnO_2 at the boundaries, where the interaction between different orbitals of SnS and SnO_2 will alter the electronic states and band structure because of the conduction band and valence band potentials.[22,31] This would be beneficial for the enhancement of charge-transfer kinetics in electrochemical reactions.[22,24] From the TGA analysis (Figure S4), the amounts of graphene and carbon in the C@SnS/SnO_2@Gr composite are about 8 wt % and 23 wt %, respectively.

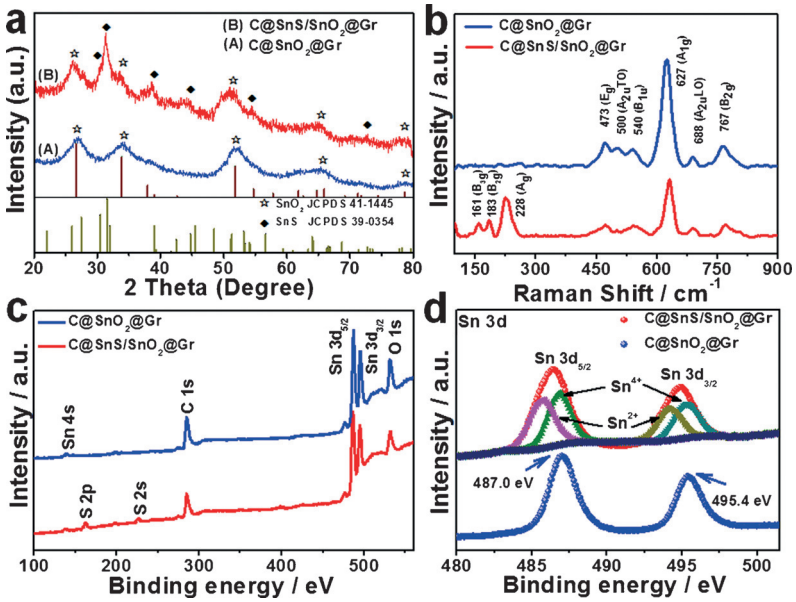

Figure 1. a) X-ray diffraction patterns of A) C@SnO_2@Gr and B) C@SnS/SnO_2@Gr. b) Room temperature Raman spectra of C@SnO_2@Gr andC@SnS/SnO_2@Gr samples. c) Typical XPS survey spectra and d) the corresponding Sn 3d XPS spectra of C@SnO_2@Gr and C@SnS/SnO_2@Gr.

The microstructure and morphology of the composites obtained were observed by scanning electron microscopy (SEM) and transmission electron microscopy (TEM). As shown

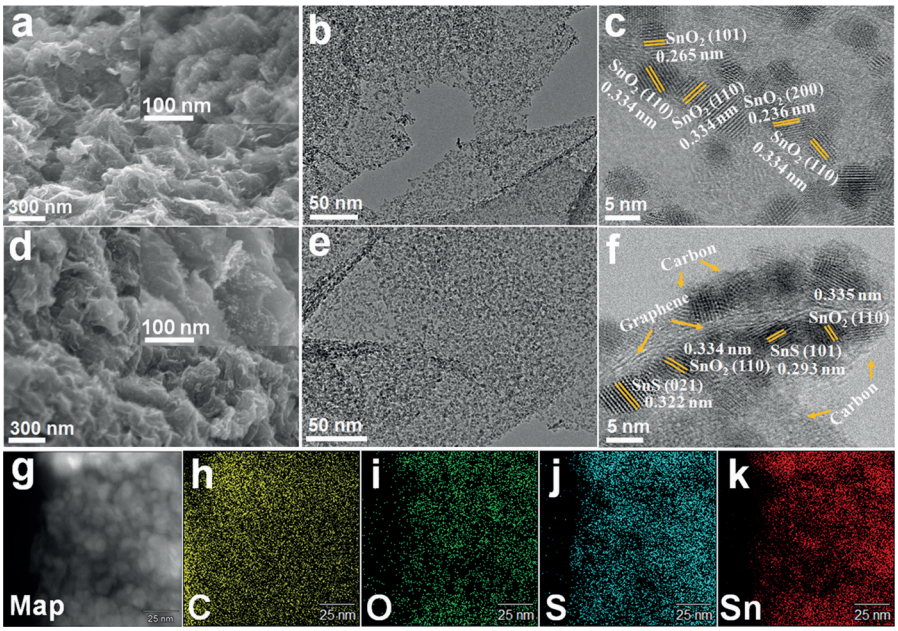

Figure 2. a) SEM image and b),c) TEM images of the C@SnO_2@Gr. d) SEM image and e),f) TEM images of the C@SnS/SnO_2@Gr. g)–k) TEM image and element mapping images of the C@SnS/SnO_2@Gr. Insets in (a) and (d) show enlarged views.

in Figure 2, both C@SnO_2@Gr (Figure 2a) and C@SnS/SnO_2@Gr (Figure 2d) have a uniform morphology over the whole surface. A large number of tiny nanoparticles (ca. 5 nm in size) are evenly distributed on graphene nanosheets (insets in Figure 2a,d), manifesting the stable structure of the C@SnO_2@Gr composite before and after the sulfidiation treatment, which is of great importance for the electrode materials in electrochemical testing. Figure 2b,e, and Figure S5 present representative TEM images of the C@SnO_2@Gr and C@SnS/SnO_2@Gr samples. It can be clearly observed that the few-layer graphene nanosheets have a great many ultrathin nanoparticles homogeneously anchored on them, which is consistent with the SEM images (Figure 2a,d). Furthermore, the TEM images reveal that the C@SnS/SnO_2@Gr and C@SnO_2@Gr almost have the same morphology, which can further demonstrate the stability of the complex structure during the sulfidation reaction. The high-resolution TEM (HRTEM) image of the C@SnS/SnO_2@Gr hybrid (Figure 2f) demonstrates the formation of SnS/SnO_2 nano-heterostructures. The lattice fringes of about 0.335 nm and 0.265 nm, respectively correspond to the (110) and (101) planes of SnO_2,[26] while the interatomic spacings of 0.293 nm and 0.322 nm correspond to the (101) and (021) planes of SnS.[29,32] Both the SnS and the SnO_2 nanoparticles are in tight contact with each other and form heterojunctions in the interfacial area, which can enhance electronic conductivity and rapid ion/electron transfer.[25] Moreover, it is also interesting to see that the few-layer graphene nanosheets support the SnS and SnO_2 nanoparticles, while the carbon layer forms a coating at the outer edge, which can not only provide an effective buffer matrix for the SnS/SnO_2 nanoparticles to relieve the volume changes and maintain the structural integrity, but also improves the conductivity. The elemental mapping (Figure 2h–k) unambiguously confirms the presence of C, O, S, and Sn elements in the C@SnS/SnO_2@Gr. The S and O elements are homogeneously distributed, which illustrates the in situ formation of SnS in the SnO_2 matrix, resulting in the intimate contact of the two components and the formation of heterostructures.

Cyclic voltammetry (CV) was employed to investigate the Na-ion storage behavior of the materials (Figure 3a, Figure S6). During the first reduction process, a clear reduction peak appeared at approximately 0.75 V, which disappeared in the following negative scan, a result of the formation of the solid electrolyte interface film.[13] From the 2nd cycle, three pairs of oxidation/reduction peaks, localized at 0.08 V/0 V, 0.23 V/0.15 V, and 0.73 V/0.68 V, appeared and remained stable, corresponding to the alloying/dealloying reactions.[13] The reduction peak at approximately 1.06 V in the CV curves can be ascribed to the conversion reaction of SnS, while the oxidation peak localized at about 1.15 V corresponds to the back-conversion of Sn and Na_2S into the SnS phase. It is noteworthy that the CV curves almost overlap from the 2nd to the 5th cycles, reflecting the highly reversible nature of the electrochemical reactions in the C@SnS/SnO_2@Gr anode and ensuring prolonged cycling stability.

The electrochemical performance of the electrodes was evaluated by galvanostatic discharge–charge measurements (Figure 3, Figure S7). The C@SnS/SnO_2@Gr composite shows a first discharge capacity of 976 $mA\,h\,g^{-1}$ and a charge capacity of 729 $mA\,h\,g^{-1}$ at 30 $mA\,g^{-1}$ (Figure 3b,c), corresponding to an initial coulombic efficiency of 74.6%. In contrast, the first cycle efficiency of the C@SnO_2@Gr is only 41.3%, and the C@SnS@Gr exhibited a stable capacity of 637 $mA\,h\,g^{-1}$ after 10 cycles (Figure 3c,d). The C@SnS/SnO_2@Gr anode displays a higher reversible capacity than the C@SnO_2@Gr or C@SnS@Gr materials, which can be attributed to the synergistic effects of SnS/SnO_2.[25] After 70 cycles, the C@SnS/SnO_2@Gr electrode achieves a reversible capacity of 713 $mA\,h\,g^{-1}$ with approximately 98% capacity retention. Figure 3c shows the rate capability of all the prepared electrodes from 30 $mA\,g^{-1}$ to 7290 $mA\,g^{-1}$. As can be seen clearly, the C@SnS/SnO_2@Gr electrode features superior high-rate performance. On increasing the current density to 810 and 2430 $mA\,g^{-1}$, the specific capacity at these current densities is still 520 and 430 $mA\,h\,g^{-1}$, respectively, which is much higher than for the C@SnO_2@Gr or C@SnS@Gr or a mechanical mixture of them (C@SnS + SnO_2@Gr). Figure 3e presents the long-term cycling performance of the C@SnS/SnO_2@Gr electrode when discharged/charged at high current densities. It can still deliver a discharge

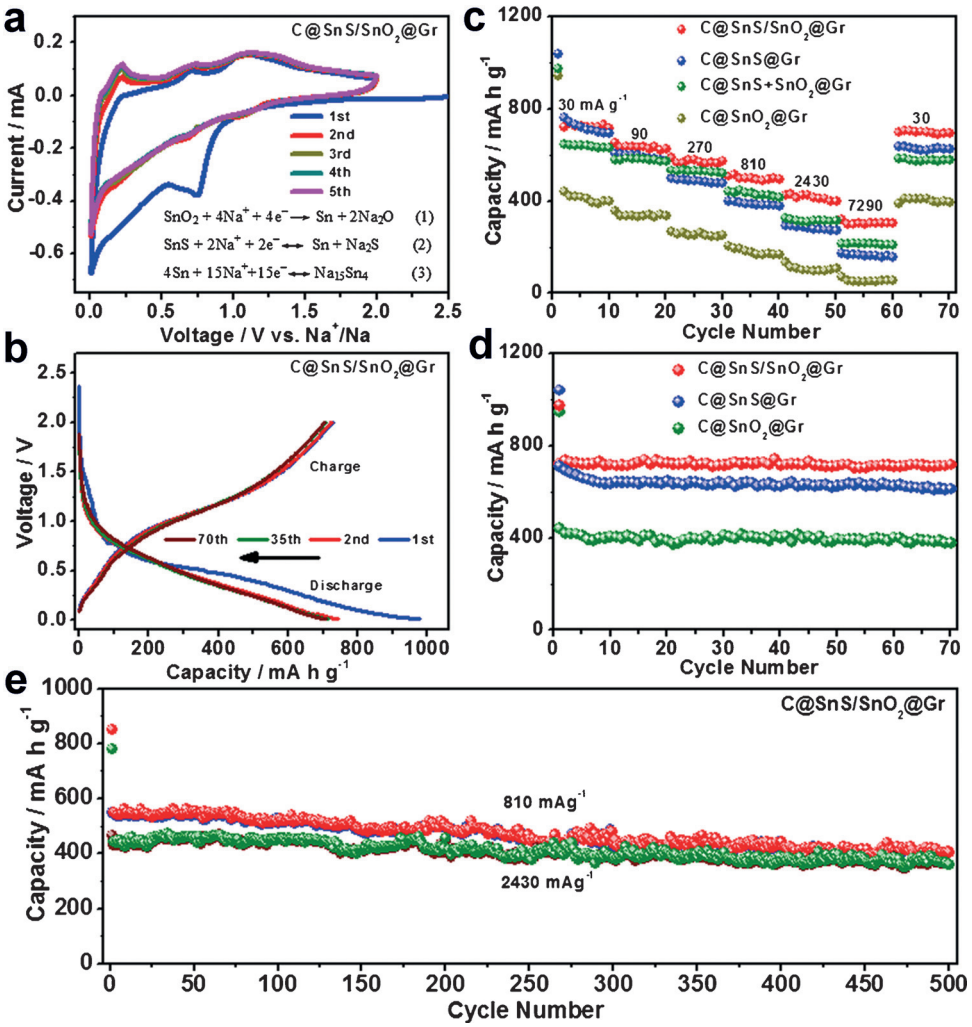

Figure 3. Electrochemical performance of C@SnS/SnO_2@Gr sample for sodium storage. a) Cyclic voltammograms for the first five cycles of the C@SnS/SnO_2@Gr electrode at a scanning rate of 0.1 mVs^{-1}. b) Galvanostatic discharge-charge profiles for selected cycles of the C@SnS/SnO_2@Gr electrode at 30 $mA\,g^{-1}$. c) Rate capabilities of C@SnS/SnO_2@Gr, C@SnS@Gr, C@SnO_2@Gr, and C@SnS + SnO_2@Gr electrodes. d) Cycling performance of C@SnS/SnO_2@Gr, C@SnS@Gr, and C@SnO_2@Gr at 30 $mA\,g^{-1}$, and e) long-term cycling performance of the C@SnS/SnO_2@Gr electrode at different current densities.

capacity of 409 $mA\,h\,g^{-1}$ after 500 cycles at 810 $mA\,g^{-1}$ (ca. 73% retention), implying excellent cycling stability (Figure S8). More importantly, even after 500 cycles at 2430 $mA\,g^{-1}$, a reversible capacity close to 360 $mA\,h\,g^{-1}$(ca. 76% retention) is still obtainable, indicating the superior high-rate cycling stability of C@SnS/SnO_2@Gr (Figure S9). The significantly improved Na^+ storage performance might be related to the synergetic enhancement of electron and sodium-ion transport kinetics, benefiting from the internal electric field within the nanoparticles.[22,25] Furthermore, the in situ generation of SnS nanoparticles in the SnO_2 matrix can effectively immobilize the SnO_2, thus reducing the self-agglomeration of SnO_2 nanocrystals and maintaining good structural stability.[33] We also compare the rate performance of the C@SnS/SnO_2@Gr electrode in this work with the state-of-the-art results in previously published papers on SnO_2-, SnS-, SnS_2- and Sn-based systems (Table S1). The capacity and high-rate performance of the C@SnS/SnO_2@Gr composite is greatly superior to those of most reported anodes for Na-ion batteries. Such excellent performance shows that the as-prepared C@SnS/SnO_2@Gr composite has great potential as the anode in applications for Na-ion batteries.

Electrochemical impedance spectroscopy (EIS) measurements were performed to research the kinetic differences between various electrodes. Both of the Nyquist plots shown in Figure S10 present depressed semicircles in the high-medium frequency region and an inclined line in the low frequency region. Of note is that the semicircle diameter for C@SnS/SnO_2@Gr is much smaller than that for C@SnO_2@Gr, C@SnS@Gr, and C@SnS + SnO_2@Gr, indicating enhanced electron- and sodium-ion transport after the formation of the SnS/SnO_2 heterostructures. The reduced charge-transfer impedance will increase the electrode kinetics and consequently improve the high-rate performance of the C@SnS/SnO_2@Gr electrode.

Based on the above results, a possible mechanism for the enhancement of the Na^+ storage performance was proposed, as shown in Scheme 2. In our system, SnO_2 is an n-type semiconductor with a wide band gap of 3.8 eV, while SnS works as a narrow-band-gap (1.3 eV) p-type semiconductor. Therefore, the SnS/SnO_2 p–n heterojunctions that are formed will induce a built-in electric field on the heterointerfaces, which will greatly accelerate the charge-transfer kinetics and result in high-rate capability. This is confirmed by the much lower charge-transport/diffusion resistance in the C@SnS/SnO_2@Gr electrode (Figure S10). During the discharging process, the direction of the electric field induced by the p–n heterojunction will point to SnS from the SnO_2 surface. Under this electric field, the charge accumulation layer at the interface is subjected to breakdown, and Na^+ diffusion in the bulk will become much easier, thus helping the Na^+ insertion.[34] After full sodiation, SnO_2 is changed into Na_xSn and Na_2O, whereas SnS is converted into Na_xSn and Na_2S. During the charge process, SnS micro-domain can release much more

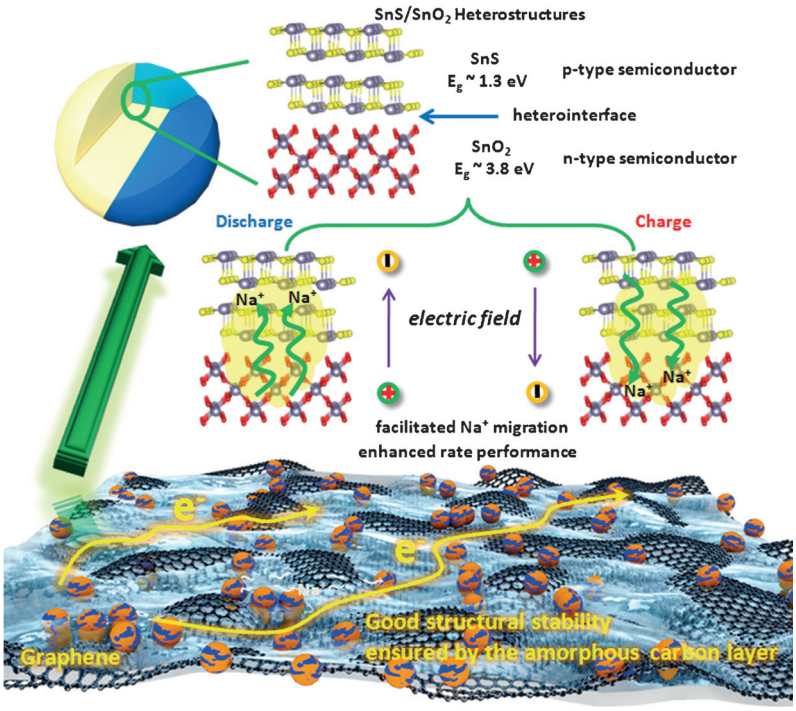

Scheme 2. Summary of the enhanced high-rate capacity mechanism of the C@SnS/SnO_2@Gr in the Na-ion battery system.

Na^+ owing to its higher reversibility than SnO_2 microdomain.[31,32] In this case, a Na^+-rich region will form in the SnS phase and a Na^+-poor area in the SnO_2 phase. Because of the potential difference, it will induce a new electric field at the interface with a direction from SnS to SnO_2, which will facilitate Na^+ migration, promoting Na^+ extraction in the charge process. Furthermore, the structural and electrical integrity of the electrode via the interfacial amorphous carbon layer anchoring the SnS/SnO_2 nanoparticles to the graphene also play important roles in improving the electrochemical performance. Therefore, the outstanding performance can be ascribed to the following reasons: 1) the charge-transfer driving force originating from the SnS/SnO_2 nanoheterostructures; 2) the higher initial coulombic efficiency and reversible capacity provided by the SnS nanoparticles; 3) the short ion-diffusion paths due to the ultra-small nanoparticles; 4) the good structural stability and excellent electrical conductivity ensured by the carbon layer and the graphene network.

In conclusion, an effective approach, involving an interfacial amorphous carbon layer anchoring SnS/SnO_2 heterostructures directly to graphene nanosheets, has been developed. The formation of the SnS/SnO_2 heterostructures has been verified by HRTEM, Raman, and XPS analysis. When evaluated as an anode material for sodium-ion batteries, the C@SnS/SnO_2@Gr features excellent performance and outstanding cycling stability at high rates, which is much superior to the performance of C@SnO_2@Gr, C@SnS@Gr, or a mechanical mixture of them. The boosted charge transfer in the heterostructures is demonstrated by the EIS measurements. The resulting improvement of Na-ion diffusion capability and electronic conductivity is mainly responsible for the extraordinary performance of the C@SnS/SnO_2@Gr electrode. The superior high-rate capability and ultra-long cycle life, accompanied by the simplicity of the synthetic process, make this approach a promising strategy for the development of simple and universal synthesis methods in applications for energy storage and conversion.

Acknowledgements

Financial support provided by the Australian Research Council (ARC) (DP1094261 and FT150100109) is gratefully acknowledged. We also thank the Electron Microscopy Centre (EMC) at the University of Wollongong. We thank K. Huang, Y.J. Liu, H. Gao, and S.D. Min for their help and thank Dr. T. Silver for critical reading of the manuscript.

Keywords: heterostructures · high rate capability · SnO_2 · SnS · sodium-ion batteries

How to cite: *Angew. Chem. Int. Ed.* **2016**, *55*, 3408–3413
Angew. Chem. **2016**, *128*, 3469–3474

[1] X. Fan, J. Mao, Y. Zhu, C. Luo, L. Suo, T. Gao, F. Han, S. Liou, C. Wang, *Adv. Energy Mater.* **2015**, *5*, 1500174.
[2] H. Yu, Y. Ren, D. Xiao, S. Guo, Y. Zhu, Y. Qian, L. Gu, H. Zhou, *Angew. Chem. Int. Ed.* **2014**, *53*, 8963–8969; *Angew. Chem.* **2014**, *126*, 9109–9115.
[3] J. Liu, P. Kopold, C. Wu, P. Aken, J. Maier, Y. Yu, *Energy Environ. Sci.* **2015**, *8*, 3531–3538.
[4] S. Ong, V. Chevrier, G. Hautier, A. Jain, C. Moore, S. Kim, X. Ma, G. Ceder, *Energy Environ. Sci.* **2011**, *4*, 3680–3688.
[5] X. Zhou, Y. Zhong, M. Yang, M. Hu, J. Wei, Z. Zhou, *Chem. Commun.* **2014**, *50*, 12888–12891.
[6] W. Li, S. Chou, J. Wang, J. Kim, H. Liu, S. Dou, *Adv. Mater.* **2014**, *26*, 4037–4042.
[7] L. Wu, X. Hu, J. Qian, F. Pei, F. Wu, R. Mao, X. Ai, H. Yang, Y. Cao, *Energy Environ. Sci.* **2014**, *7*, 323–328.
[8] L. Pei, Q. Jin, Z. Zhu, Q. Zhao, J. Liang, J. Chen, *Nano Res.* **2015**, *8*, 184–192.
[9] Y. Zhao, C. Wei, S. Sun, L. Wang, Z. Xu, *Adv. Sci.* **2015**, *2*, 1500097.
[10] Y. Zhang, J. Xie, S. Zhang, P. Zhu, G. Cao, X. Zhao, *Electrochim. Acta* **2015**, *151*, 8–15.
[11] Z. Li, J. Ding, H. Wang, K. Cui, T. Stephenson, D. Karpuzov, D. Mitlin, *Nano Energy* **2015**, *15*, 369–378.
[12] Y. Wang, Y. Lim, M. Park, S. Chou, J. Kim, H. Liu, S. Dou, Y. Kim, *J. Mater. Chem. A* **2014**, *2*, 529–534.
[13] T. Zhou, W. Pang, C. Zhang, J. Yang, Z. Chen, H. Liu, Z. Guo, *ACS Nano* **2014**, *8*, 8323–8333.
[14] C. Zhu, P. Kopold, W. Li, P. Aken, J. Maier, Y. Yu, *Adv. Sci.* **2015**, *2*, 1500200.
[15] J. Huheey, E. Keiter, R. Keiter in *Inorganic Chemistry: Principles of Structure and Reactivity*, Harpercollins College Publishers, New York, **1993**, pp. 138–251.

[16] L. Wu, H. Lu, L. Xiao, J. Qian, X. Ai, H. Yang, Y. Cao, *J. Mater. Chem. A* **2014**, *2*, 16424 – 16428.
[17] Y. Denis, P. Prikhodchenko, C. Mason, S. Batabyal, J. Gun, S. Sladkevich, A. Medvedev, O. Lev, *Nat. Commun.* **2013**, *4*, 2922.
[18] C. Bommier, X. Ji, *Isr. J. Chem.* **2015**, *55*, 486 – 507.
[19] X. Zhu, N. Monahan, Z. Gong, H. Zhu, K. Williams, C. Nelson, *J. Am. Chem. Soc.* **2015**, *137*, 8313 – 8320.
[20] P. Zubko, S. Gariglio, M. Gabay, P. Ghosez, J. Triscone, *Annu. Rev. Condens. Matter Phys.* **2011**, *2*, 141 – 165.
[21] C. Huang, S. Wu, A. Sanchez, J. Peters, R. Beanland, J. Ross, P. Rivera, W. Yao, D. Cobden, X. Xu, *Nat. Mater.* **2014**, *13*, 1096 – 1101.
[22] X. Chang, T. Wang, P. Zhang, J. Zhang, A. Li, J. Gong, *J. Am. Chem. Soc.* **2015**, *137*, 8356 – 8359.
[23] X. Hong, J. Kim, S. Shi, Y. Zhang, C. Jin, Y. Sun, S. Tongay, J. Wu, Y. Zhang, F. Wang, *Nat. Nanotechnol.* **2014**, *9*, 682 – 686.
[24] J. Nishitani, K. Yu, W. Walukiewicz, *Appl. Phys. Lett.* **2014**, *105*, 132103.
[25] J. Wang, Y. Zhou, Z. Shao, *Electrochim. Acta* **2013**, *97*, 386 – 392.
[26] C. Zhang, X. Peng, Z. Guo, C. Cai, Z. Chen, D. Wexler, S. Li, H. Liu, *Carbon* **2012**, *50*, 1897 – 1903.
[27] J. Cheng, H. Xin, H. Zheng, B. Wang, *J. Power Sources* **2013**, *232*, 152 – 158.
[28] M. Liu, J. Yang, Q. Qu, P. Zhu, W. Li, *J. Power Sources* **2015**, *273*, 848 – 856.
[29] S. Sohila, M. Rajalakshmi, C. Ghosh, A. Arora, C. Muthamizhchelvan, *J. Alloys Compd.* **2011**, *509*, 5843 – 5847.
[30] M. Fondell, M. Gorgoi, M. Boman, A. Lindblad, *J. Electron Spectrosc. Relat. Phenom.* **2014**, *195*, 195 – 199.
[31] D. Jiang, L. Chen, J. Zhu, M. Chen, W. Shi, J. Xie, *Dalton Trans.* **2013**, *42*, 15726 – 15734.
[32] J. Ning, K. Men, G. Xiao, L. Wang, Q. Dai, B. Zou, B. Liu, G. Zou, *Nanoscale* **2010**, *2*, 1699 – 1703.
[33] I. Kim, J. Seo, S. Oh, S. Patil, S. Hwang, *Adv. Funct. Mater.* **2015**, *25*, 4948 – 4955.
[34] T. Zhou, Y. Zheng, H. Gao, S. Min, S. Li, H. Liu, Z. Guo, *Adv. Sci.* **2015**, *2*, 1500027.

Received: November 30, 2015
Published online: February 4, 2016

